Optics Letters

V-shaped PSF for 3D imaging over an extended depth of field in wide-field microscopy

Yunyang Li,[1,†] Zixiao Zhang,[1,†] Feng Tian,[1] Yryx Y. Luna-Palacios,[2] Israel Rocha-Mendoza,[2] and Weijian Yang[1,*]

[1]Department of Electrical and Computer Engineering, University of California, Davis, California 95616, USA
[2]Centro de Investigación Científica y de Educación Superior de Ensenada, Carretera Ensenada-Tijuana 3918, Ensenada B.C. 22860, Mexico
[†]These authors contributed equally to this work.
[*]wejyang@ucdavis.edu

Received 10 October 2024; revised 18 November 2024; accepted 25 November 2024; posted 2 December 2024; published 8 January 2025

Single-shot 3D optical microscopy that can capture high-resolution information over a large volume has broad applications in biology. Existing 3D imaging methods using point-spread-function (PSF) engineering often have limited depth of field (DOF) or require custom and often complex design of phase masks. We propose a new, to the best of our knowledge, PSF approach that is easy to implement and offers a large DOF. The PSF appears to be axially V-shaped, engineered by replacing the conventional tube lens with a pair of axicon lenses behind the objective lens of a wide-field microscope. The 3D information can be reconstructed from a single-shot image using a deep neural network. Simulations in a 10× magnification wide-field microscope show the V-shaped PSF offers excellent 3D resolution (<2.5 μm lateral and ∼15 μm axial) over a ∼350 μm DOF at a 550 nm wavelength. Compared to other popular PSFs designed for 3D imaging, the V-shaped PSF is simple to deploy and provides high 3D reconstruction quality over an extended DOF.

https://doi.org/10.1364/OL.544552

In biological imaging, capturing detailed 3D volumes is essential for understanding complex structures and processes. High-speed volumetric imaging is crucial for applications like studying brain activity in neural circuits [1,2] or visualizing macroscopic cleared samples [3]. Conventional microscopes, limited to single-plane imaging, are unsuitable for these tasks. Spatial multiplexing techniques can image different depths at once but require complex optical setups and have an inefficient photon use [4–6]. Extended depth-of-field (DOF) techniques with elongated point spread functions (PSFs) in the axial direction can capture volumetric information at once [7–10]. However, common low numerical aperture (NA) Gaussian and Bessel beam PSFs, lack axial variance and cannot distinguish features at different depths [7–9].

PSF engineering [11] enables single-shot 3D imaging by shaping the PSF to remain spatially confined while varying its profile along the depth, typically by an amplitude [12] or phase mask [11,13–15] at the Fourier plane of the microscope. Techniques like astigmatic PSF [16], double helix [13,14], and single helix [15] can capture 3D information in one acquisition. Meanwhile, the optimized tetrapod PSF [17] and the light-field microscopy with a microlens array at the image plane [18] enable 3D imaging. However, these methods are often designed for applications with a limited axial range, or require a custom and often complex design of phase masks. High resolution imaging over a large depth of field remains a general challenge.

In this Letter, we report a V-shaped PSF that resolves 3D information in high resolution over an extended DOF in wide-field microscopy. The V-shaped PSF is formed by two spatially separated and angled Bessel beams. A single object is imaged as two spatially displaced copies on the 2D image plane, with a separation distance proportional to the object depth. Crucially, each lobe of the PSF stays spatially confined over an extended DOF, making it possible to resolve 3D features over a large DOF. Compared to many other PSFs for 3D imaging, the V-shaped PSF is easy to implement and achieves a higher 3D reconstruction quality over an extended DOF range. A self-bending PSF, in a V-shape, has been demonstrated previously with a spatial light modulator [19], requiring a complex optical setup, precise polarization tuning, and system calibration. Instead, our PSF can be generated in wide-field microscopy by replacing the tube lens with two laterally displaced axicon lenses (Fig. 1) or by adding another tube lens and the axicon lenses (Note 1 and Fig. S1 in Supplement 1). The volumetric object is projected into a single 2D image and algorithms like the Richardson–Lucy deconvolution or deep neural networks can reconstruct the 3D object. As a proof of concept, we designed the double-axicon lens for a 10× (0.25 NA, with ∼20 μm native DOF) microscope objective lens to form the V-shaped PSF at 550 nm wavelength. Simulations show good lateral <2.5 μm and axial ∼15 μm resolutions over an ∼350 μm DOF. Using a deep neural network, we reconstruct 3D objects in high quality with high intersection over union (IOU) against the ground truths. We show that the V-shaped PSF achieves high 3D reconstruction quality over an extensive DOF, comparable to the numerically optimized PSF for 3D imaging, while offering a much simpler design and implementation.

Double-axicon lens to generate V-shaped PSF. The V-shaped PSF is formed by two tilted Bessel beams, each with a

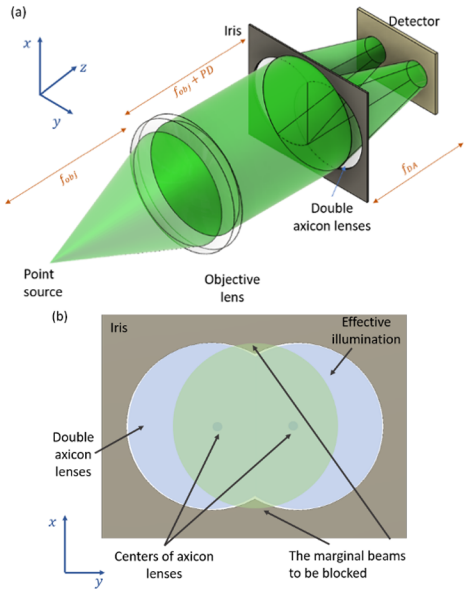

Fig. 1. Double-axicon lenses to generate the V-shaped PSF. (a) Schematic of the 3D extended DOF microscope with an objective lens and double-axicon lenses (drawing not to scale). An iris in front of the double-axicon lenses rejects the marginal beams. The double-axicon lenses serve as a tube lens, with the detector plane at their nominal rear focal plane. A V-shaped PSF is formed with the two lobes separation varying with object distance. (b) Front view of the double-axicon lenses and illumination beam.

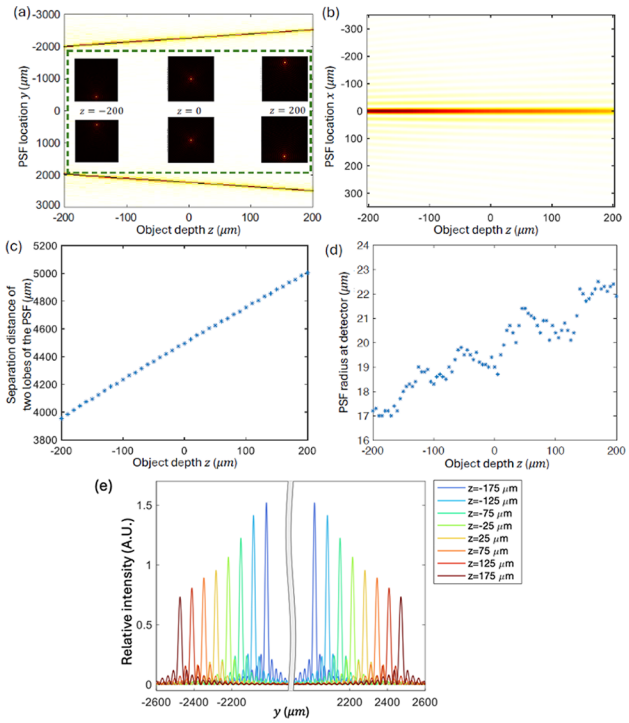

Fig. 2. (a) and (b) Simulation of the V-shaped PSF. Illustration of the two PSF lobes imaged by the camera versus the depth of the on-axis object point source in the (a) yz plane and (b) xz plane intersecting the PSF's maximum value. Inset of (a), intensity profile of the two main PSF lobes in the xy plane for three object depths. (c) Separation of the two PSF lobes versus object depth. (d) Radius of the PSF main lobes versus object depth. The discontinuity quantization effect is due to the detector pixelation and numerical simulation precision. (e) The lateral PSFs (along the y-direction) at different object depths within the 350 μm DOF. PSF intensity is normalized to the PSF at the nominal focal plane. As the object point source moves toward the objective lens, more marginal beams are blocked by the iris at the axicon plane, resulting in a reduced transmission power.

central lobe that remains spatially confined over a long distance. The PSF is generated by replacing the tube lens in a wide-field microscope with a pair of axicon lenses positioned adjacently (Fig. 1(a), Note 2 in Supplement 1). Alternatively, another tube lens and a pair of axicon lenses can be added between the original tube lens and camera (Note 1 and Fig. S1 in Supplement 1). The pupil distance (PD) between the axicon lenses and the pupil plane of the objective lens (Fig. 1(a)) is selected for high transmission efficiency over the extended DOF while maintaining a low distortion (±3% at the edge of a 700 μm × 700 μm FOV over a 350 μm DOF). The nominal focal length of the axicon lens is given by $f = R/[2(n\text{-}1)\alpha]$, where R is the radius of the axicon, n is the refractive index of the lens material, and α is the tilting angle of the conical shape [9]. f can be set to be the same as that of the tube lens to be replaced. We set the diameter of the axicon lens to be the same as that of the pupil of the microscope and the separation of the two axicon lenses to be the radius of the axicon lens to achieve high transmission efficiency while minimizing the material cost (Fig. 1(b)). An iris at the axicon plane ensures only light passing through the axicon lenses reaches the detector (~92% transmission). A camera at the nominal rear focal plane of the double axicon lens collects two copies of images with a separation dependent on the object depth.

We paired the double-axicon lenses with a 10× magnification microscope objective lens (0.25 NA). The effective focal length of the objective lens was set to be f_{obj} = 18 mm, with a pupil diameter $D = 2 \cdot \text{NA} \cdot f_{obj}$ = 9 mm. The axicon lenses were designed with a focal length of f_{DA} =180 mm and a diameter of 9 mm to create 10× magnification and maximize light transmission. The centers of the axicon lenses were separated by 4.5 mm. Their small overlap creates some asymmetricity in the PSF lobes and slightly alters the focal length of the double axicon, but it has impact on the 3D resolving capability and DOF.

System characteristics. We investigated the imaging system's performance using a ray-tracing algorithm (Zemax OpticStudio). We placed an object point source along the optical axis and monitored the PSF on the detection plane (Figs. 2(a)–2(b)). As the axial position z of the point source varies, the separation $2l$ of the PSF's two lobes changes approximately linearly (Fig. 2(c)), in a ratio of $\Delta(2l) / \Delta z \approx 2.62$, where l is the lateral distance between each PSF lobe and the optical axis. The PSF observed at the detector plane adopts the V-shaped form as object depth varies (Fig. 2(a) inset). The NA of each PSF lobe is approximately 0.125 and 0.25 in the y- and x-directions, respectively (Fig. 1). Over an axial distance of 350 μm of the point source, the full width at half maximum (FWHM) of each PSF lobe is <25 μm (Fig. 2(d)) in the y-direction at the detector, corresponding to <2.5 μm lateral resolution on the object plane. We defined the axial resolution as the minimum displacement of a point source in the axial direction needed to distinguish a noticeable difference in each lobe at the detector plane along the y-direction. According to the Rayleigh criteria, the axial resolving power was calculated to be ~15 μm.

As the point source moves toward the objective lens, the iris blocks more marginal beams leading to vignetting and a reduced intensity (Fig. 2(e)). Within ±175 μm axial offset from the nominal focal plane, the minimum peak intensity of the PSF is ~50% of the maximum. This defines a DOF of 350 μm, much larger than the native DOF of the objective lens (~20 μm), or when two convex lenses with the same focal length are used instead of the two axicon lenses (<30 μm DOF to keep a similar lateral resolution as the double axicon lens, simulated by OpticStudio). While the Bessel beams extend the DOF, the central lobe contains significantly less energy as the number of rings increases, all with a uniform distribution [20,21]. The lower energy density in the outer rings limits their effectiveness for fluorescence detection. Therefore, we expect that primarily the central lobe and those rings exceeding the camera's detection threshold will contribute meaningfully to object detection and reconstruction. We further studied the properties of the V-shaped PSF when the double axicon lens is laterally shifted or tilted, which mimics real experiment conditions (Note 3 and Fig. S2–S5 in Supplement 1). Based on the 3D PSF, we proposed approaches to finely align the double axicon lens in the microscope.

3D image reconstruction. The microscope with the V-shaped PSF projects the 3D object space into a 2D image on the camera. With prior knowledge of the PSF (Fig. 2(a)), we can reconstruct the 3D object volume from a single 2D image. Conventional reconstruction algorithms (e.g., the Richardson–Lucy deconvolution and the fast iterative shrinkage-thresholding algorithm [22]) are time-consuming and computationally intensive for highly compressed images or when the number of the reconstruction pixel/voxel is large. Deep neural networks, once trained, could offer faster run times and can learn regularization terms to enhance reconstruction quality. Here, we adopted a deep neural network based on Hadamard-Nets [23–26], which has proven robust and efficient for object reconstruction. The network comprises a learnable deconvolution module to reconstruct all the axial planes at once, and a 3D U-Net, to refine and fuse the reconstruction from different depths (Note 4 and Fig. S6 in Supplement 1). The deconvolution module uses a physics-informed multi-Hadamard-Net [25,26], where each Hadamard-Net learns the deconvolution kernel for a specific axial depth in frequency domain. The network broadcasts the Fourier transform of the measured image to N pairs, where N is the number of axial planes to be reconstructed. Each pair contains the real and imaginary components, which are respectively elementwise multiplied with a pair of learnable Hadamard kernels. Each pair of learned Hadamard kernels extracts object features from one axial depth. The product is then inverse-transformed to the spatial domain and stacked into a 3D volume with N depths. In the fusion module, a 3D U-Net is used to post-process the volume to suppress the background and remove duplicated out-of-focus features that appear on multiple depths. The fusion network outputs an N-depth 3D volume. As a proof of concept, we set N = 8 here.

We used neuronal imaging in transparent samples (i.e., zebrafish *in vivo* or 3D cleared samples), as an example. We constructed a database for 3D object planes with randomly distributed neuronal cell bodies (~8 μm in diameter; see Fig. 3(a)). To resemble the 2D image as would be taken in the experiment, we convolved the object at various depths with the PSF generated by Zemax OpticStudio with calibrated magnification, added with 5% Gaussian noise (related to amplifier noise and read noise of the camera) and 5% Poisson noise (related to shot noise). We

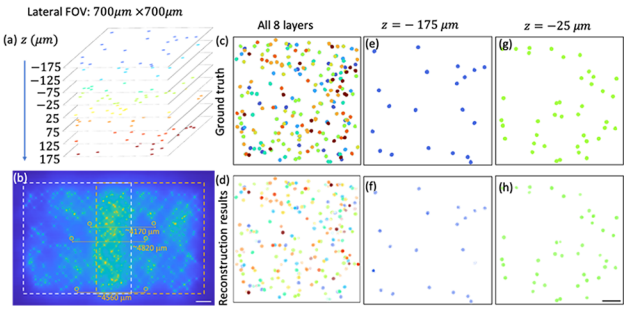

Fig. 3. 3D imaging and reconstruction of eight evenly distributed object planes with neuronal cell bodies across 350 μm DOF. (a) Ground truth of the eight planes within 350 μm DOF with different colors for neuronal cell bodies at different depths. The FOV of each plane is 700 μm × 700 μm and the cell bodies have an average diameter of 8 μm. (b) Image of the eight planes through the V-shaped PSF at the camera. The yellow circles show double images of the same neurons with separation depending on depth. Dashed boxes indicate the sensor regions for the images from the two PSF lobes, which may overlap if the FOV of the individual PSF lobe is large. (c) Same as (a), but with all planes projected into a 2D view. (d) Reconstruction results at the eight planes, shown in 2D projection. (e) Ground truth and (f) reconstruction at z = −175 μm plane. (g) and (h) Same as (e) and (f), but for z = −25 μm plane. In (d), (f), and (h), the gray-scaled color indicates the relative intensity among the neurons in the reconstruction. Scale bar: (b) 1 mm; (h) 100 μm.

then summed images from different depths into a single image (Fig. 3(b)). The same cells appear to be imaged twice due to the V-shaped PSF, with their lateral separation depending on the cell depth. The single images and corresponding object planes were used as training pairs for the neural network reconstruction at different depths.

We evaluated the reconstruction performance for a volume with eight evenly distributed object planes within the 350 μm DOF (Fig. 3) to simulate the multiplane light-sheet illumination where a set of selected planes are illuminated [27]. Each object plane is 700 μm × 700 μm. The neuronal cell bodies were well reconstructed with an averaged IOU of 0.65 between the ground truth and the reconstructed image. The reconstruction time for eight planes is ~35 ms (NVIDIA GeForce RTX 2080 Ti). While this example illuminated selected planes with separation distances larger than the axial resolution, our algorithm can handle the case where the entire volume is illuminated (Note 5 and Fig. S7 in Supplement 1). Our deep neural network, while trained for a small range of neuronal density, can work for a wider range of neuronal density though in a reduced performance (Note 6 and Figs. S8 and S9 in Supplement 1).

We also benchmarked the reconstruction performance of the V-shaped PSF over other popular PSFs engineered for 3D imaging using the same neural network architecture (Fig. 4, Note 7 and Figs. S10–S12 in Supplement 1). These PSFs include the conventional diffraction-limited PSF (DL-PSF), the astigmatic PSF [16], the double-helix PSF [13,14], and the tetrapod PSF [17]. All PSFs were designed with the same NA and aperture size. The tetrapod PSF was numerically optimized through the Cramer–Rao lower bound (CRLB) metric [11,17] over the same ± 175 μm DOF as the V-shaped PSF.

Using the same methodology in Fig. 3, we assessed the reconstruction quality for eight evenly distributed object planes within

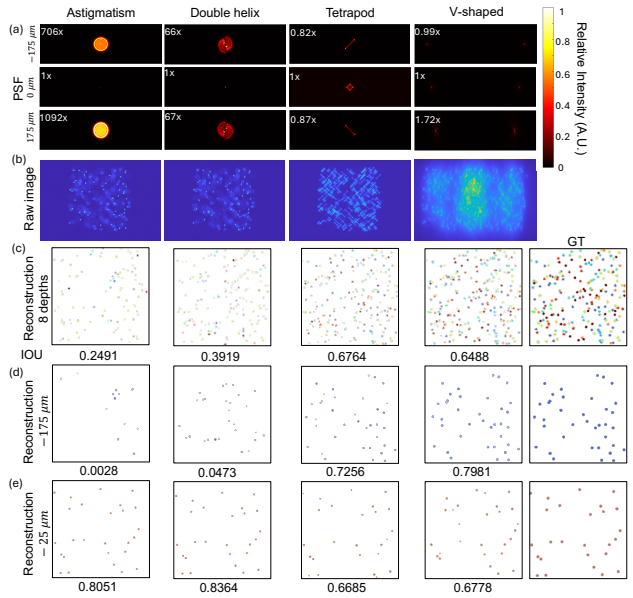

Fig. 4. A comparison of the image reconstruction performance of different PSFs (astigmatic, double-helix, tetrapod, and V-shaped) using the same neural network architecture. The samples were neuronal cell bodies randomly distributed in eight evenly separated object planes across a 350 μm DOF. (a) Lateral PSFs at −175 μm, 0 μm, and 175 μm depths. The peak intensity of each PSF is scaled to (0,1) for visualization, with the corresponding scaled factor noted. (b) Raw measured images generated by each PSF technique using the same sample. (c)–(e) Reconstruction results for (c) all eight depths, (d) plane −175 μm, and (e) plane −25 μm. The intersection over union (IOU) between the reconstruction results and the ground truth is noted as the average value for (c) all eight depths, (d) plane −175 μm, and (e) plane −25 μm. The ground truth images are displayed on the right. See Fig. S11 in Supplement 1 for an enlarged version of this figure.

a 350 μm DOF, each plane with a 700 μm × 700 μm FOV containing 20–40 neurons. Though the reconstruction quality of the V-shaped PSF is not the best around the nominal focus, it outperforms the DL-PSF, the astigmatic PSF and the double-helix PSF over the extensive DOF (Fig. S12 in Supplement 1), attributed to its tight focusing. The V-shaped PSF performs similarly to the tetrapod PSF, which is specifically optimized for this DOF. Crucially, the V-shaped PSF can be designed intuitively without complex numerical optimization and be implemented easily.

Summary and discussion. In summary, we propose a simple-to-implement V-shaped PSF for wide-field microscopy, facilitating single-shot volumetric imaging with 3D resolution across an extended DOF. The PSF exhibits a spatially confined and depth-dependent shape throughout the extended DOF and could be generated by replacing the conventional tube lens with a pair of axicon lenses. We designed and simulated the PSF for a 10× magnification microscope and reconstructed the images at multiple depths over a DOF of 350 μm through deep neural networks. Compared with many other 3D wide-field imaging techniques through PSF engineering, our design has a large DOF. In particular, our optical setup is simple by integrating a pair of axicon lenses in the collection path and does not require complex implementation such as that in the self-bending PSF technique [19] nor complex phase mask design such as that in the tetrapod PSF [17]. We showed that the deep neural network could recover high-quality 3D object information from the single image acquisition. Compared with other popular PSFs for 3D imaging, the V-shaped PSF presented an excellent 3D reconstruction quality with a high IOU between the reconstructed objects and the ground truth over an extended DOF.

The single-shot 3D wide-field microscope with V-shaped PSF can be equipped with wide-field volumetric illumination or integrated with multiplane light-sheet illumination [27]. It holds great promise for recording 3D biological structures or processes at high speed, such as *in vivo* neuronal imaging in transparent samples (e.g., zebrafish larvae [28]), or macroscopic cleared samples [29]. Imaging multiple planes or the entire volume together greatly increases the data acquisition speed, crucial for studying fast biological dynamics or imaging macroscopic-scale samples in high resolution.

Funding. Burroughs Wellcome Fund (CASI 1015761); National Science Foundation (CAREER 1847141); UC MEXUS-CONACYT (CN-20-123).

Disclosures. The authors declare no conflicts of interest.

Data availability. Data underlying the results presented in this Letter are not publicly available at this time but may be obtained from the authors upon reasonable request.

Supplemental document. See Supplement 1 for supporting content.

REFERENCES

1. M. B. Ahrens, M. B. Orger, D. N. Robson, *et al.*, Nat. Methods **10**, 413 (2013).
2. Y. Wan, Z. Wei, L. L. Looger, *et al.*, Cell **179**, 355 (2019).
3. H. R. Ueda, H. U. Dodt, P. Osten, *et al.*, Neuron **106**, 369 (2020).
4. S. Ram, P. Prabhat, E. S. Ward, *et al.*, Opt. Express **17**, 6881 (2009).
5. S. Abrahamsson, J. Chen, B. Hajj, *et al.*, Nat. Methods **10**, 60 (2013).
6. S. Xiao, H. Gritton, H. A. Tseng, *et al.*, Optica **7**, 1477 (2020).
7. G. Theriault, Y. D. Koninck, and N. McCarthy, Opt. Express **21**, 10095 (2013).
8. G. Theriault, M. Cottet, A. Castonguay, *et al.*, Front. Cell Neurosci. **8**, 139 (2014).
9. Z. Zhai, S. Ding, Q. Lv, *et al.*, J. Mod. Opt. **56**, 1304 (2009).
10. J. Greene, Y. Xue, J. Alido, *et al.*, Neurophotonics **10**, 044302 (2023).
11. Y. Shechtman, S. J. Sahl, A. S. Backer, *et al.*, Phys. Rev. Lett. **113**, 133902 (2014).
12. H. Wang and P. Zhao, Microfluid. Nanofluid. **22**, 30 (2018).
13. S. R. Pavani and R. Piestun, Opt. Express **16**, 22048 (2008).
14. S. R. Pavani, M. A. Thompson, J. S. Biteen, *et al.*, Proc. Nat. Acad. Sci. U. S. A. **106**, 2995 (2009).
15. O. Tzang, D. Feldkhun, A. Agrawal, *et al.*, Opt. Lett. **44**, 895 (2019).
16. B. Huang, W. Wang, M. Bates, *et al.*, Science **319**, 810 (2008).
17. E. Nehme, D. Freedman, R. Gordon, *et al.*, Nat. Methods **17**, 734 (2020).
18. M. Broxton, L. Grosenick, S. Yang, *et al.*, Opt. Express **21**, 25418 (2013).
19. S. Jia, J. C. Vaughan, and X. Zhuang, Nat. Photonics **8**, 302 (2014).
20. J. Durnin, J. J. Miceli, and J. H. Eberly, Opt. Lett. **13**, 79 (1988).
21. Y. Lin, W. Seka, J. H. Eberly, *et al.*, Appl. Opt. **31**, 2708 (1992).
22. A. Beck and M. Teboulle, SIAM J. Imaging Sci. **2**, 183 (2009).
23. F. Tian and W. Yang, Opt. Express **30**, 34479 (2022).
24. D. Deb, Z. Jiao, R. Sims, *et al.*, in *Proceedings of the 36th International Conference on Neural Information Processing Systems* Vol. 1829 (Curran Associates Inc., 2022), pp. 25224–25236.
25. F. Tian, B. Mattison, and W. Yang, "DeepLeMiN: Deep-learning-empowered Physics-aware Lensless Miniscope," bioRxiv (2024).
26. Q. Yang, R. Guo, G. Hu, *et al.*, Optica **11**, 860 (2024).
27. Z. Jiao, Z. Zhou, Z. Chen, *et al.*, Optica **10**, 239 (2023).
28. Y. Liu, S. Dale, R. Ball, *et al.*, Neurophotonics **6**, 015009 (2019).
29. E. Delage, T. Guilbert, and F. Yates, J. Cell Biol. **222**, e202307143 (2023).